Measurement of Inertial and Acoustic Waves in a Turbine Chute Rim Seal Cavity

Anna Bru Revert[1]
Rolls-Royce plc,
PO Box 3,
Bristol, BS34 7QE, UK
e-mail: Anna.BruRevert@Rolls-Royce.com

Paul F. Beard
Oxford Thermofluids Institute,
Department of Engineering Science,
University of Oxford,
Oxford, OX2 0ES, UK,
e-mail: paul.beard@eng.ox.ac.uk

John W. Chew
Thermo-Fluid Systems UTC,
University of Surrey,
Guidlford, GU2 7XH, UK
e-mail: j.chew@surrey.ac.uk

ABSTRACT

A chute rim seal cavity has been instrumented with time resolved and time-averaged pressure transducers as well as a gas concentration measurement system at the Oxford Rotor Facility. The unsteady pressure transducers were unevenly distributed along the circumference generating 15 combinations of angular spacing to conduct a phase analysis. The test operating conditions were modified through different configurations of mainstream flow, a range of rotational speeds and purge flows to obtain test data in the regimes of rotationally-driven, pressure-driven and combined ingestion. The rotating unsteady flow structures within the rim seal cavity were studied through a combination of phase analysis of dynamic pressure signals and inspection of the frequency domain. The introduction of mainstream flow (axial and swirled) increased the overall unsteadiness exciting an additional band of lower frequencies. The phase analysis revealed these were associated with acoustic waves, providing the first experimental evidence of

[1] Corresponding author for paper number GTP-22-1603: anna.brurevert@rolls-royce.com

the presence and coexistence of inertial and acoustic waves in the rim seal cavity. The interaction of the inertial and acoustic waves strongly depends on the operating conditions, and may be linked to changes in sealing effectiveness.

INTRODUCTION

The first studies investigating rim seal ingestion focused on rotationally-induced ingress, created by the disc pumping effect. Shortly after, the relevance of the pressure asymmetries in the main gas path above the cavity was acknowledged and the focus shifted towards researching externally-induced ingestion. Despite developments in computational modelling techniques, differences between experimental and numerical results were still large, indicating that other key elements were being missed. Publications then started to examine unsteady phenomena driving hot gas ingestion. The main source of unsteadiness was observed to arise from the vane and blade potential field interaction in the main gas path, but unsteady pressure fluctuations unrelated to the blade passing frequencies were detected in the rim seal region inside the cavity. The latter is the focus of this study.

Over the last two decades, unsteady computational fluid dynamics (CFD) and fast response pressure measurements have revealed that rim seal flows are subject to rotating flow modes associated with rim seal instabilities as represented in Fi. The presence of unsteady rotating flow structures provided an explanation for the predictive limitations of steady CFD and more elementary models. The drive to further understand the physics of the unsteady flow phenomena prompted a reassessment of the driving mechanisms for ingestion and stimulated new research.

LITERATURE REVIEW

An extensive investigation with a combined experimental and computational approach numerically identified an ingestion zone rotating at half the rotor speed in the unsteady simulations of Bohn *et al*. [1] which was not present in their steady results of [2]. Hills *et al.* [3] highlighted the importance of the flow unsteadiness over the ingestion process based on the misalignment between time-averaged rig measurements and the outcome from RANS simulations. Indeed, Hills *et al*. demonstrated that unsteady computations provided better agreement with the experimental data. The unsteady phenomena detected in the above publications was introduced by the vanes and blades in the main gas path. However, some studies started to mention the presence of unsteady flow features unrelated to the blade passing frequency. Roy *et al*. [4] reported a large mismatch between unsteady pressure measurements and steady CFD predictions. The source of disagreement was attributed to unsteady effects in the rim seal.

Experimentally, the presence of previously overlooked unsteady pressure fluctuations unrelated to the blade passing frequency and with a characteristic length larger than a vane or blade pitch was detected by Smout *et al*. [5]. Following the experimental evidence, unsteady simulations were conducted to corroborate whether the numerical models detected such structures. Shortly after, Cao *et al*. [6] published the first combined experimental and numerical study reporting the existence of large scale unsteady flow features in the cavity unrelated to the blade passing frequency. They were observed to span over a single vane or blade pitch and rotate slightly slower than the disc speed. The CFD results (with a bladeless annulus) indicated that ingestion was rotationally-driven rather than pressure-driven. Cao *et al*. detected a flow pattern of alternating regions of ingress and egress at the rim seal thought to arise from the interaction of the annulus and sealing flows. Nonetheless, the frequency was found to be a stronger function of the annulus flow swirl velocity than rotor speed.

Looking at the frequency spectra of high resolution pressure measurements, Roy *et al*. [7] identified a distinctive peak lower than the blade passing frequency at the rim seal region. This frequency was seen to propagate through the domain where it would be modulated by the presence of vanes and blades in the main gas path. Julien *et al*. [8] reported that when the large-scale structures appear, the pressure perturbations inside the disc space provoke a much deeper penetration of the flow during ingestion. Schädler *et al*. [9] stated that ingress/egress was required to trigger the rim seal instabilities since the phenomenon was defined by a local flow exchange.

Measurements from Roy *et al*. [7] revealed that in absence of purge flow, the large scale flow structures still appeared and represented the most energetic phenomenon in the frequency spectra, whilst the blade passing frequency contained more energy at high rates of sealing flow. This aligned with the findings of computational studies conducted independently. For example, Julien *et al*. [8] also found that high rates of sealing flow had a stabilizing effect on the cavity pressure fluctuations as it reduced the intensity and count of the unsteady flow structures. Other authors agreed with the observation that unsteady flow structures and the subsequent ingestion of mainstream flow could be mitigated or stabilised at high purge supplies (e.g. Schädler *et al*. [9], Chilla *et al*. [10]).

Inherent unsteadiness has been detected in axial clearances, chute seals, radial seals and overlap-type seals in experimental and numerical studies. After an extensive review of the available literature, Chew *et al*. [11] concluded that a lower frequency distinct peak was found in axial seals with large clearances as opposed to more complex geometries with tighter clearances. A recent study by Gao *et al*. [12] investigated the unsteady flow structures in axial, chute and radial seal arrangements with similar cavity volumes and found that the geometry of the latter restricted the radial outflow suppressing the rim seal instabilities (inertial waves). This aligns with the findings of the research from Horwood *et al*. [13] who reported that the intensity of the frequency peak corresponding to the rotating structures reduced with purge flow and was suppressed at $U_m/(\Omega b) = 0.1$ for a radial seal. On the contrary, for a chute seal the amplitude of the peak increased with larger sealing flows and slightly reduced at the same threshold of $U_m/(\Omega b) = 0.1$ [14]. These apparently opposing outcomes show the complexity of the phenomenon and sensitivity to different parameters such as geometrical arrangement.

The initial study by Cao *et al*. [6] found that the length-scale and strength of the unsteady 3D effects was linked to the dimensions of the cavity (radial extent, axial spacing and gap size). Town e*t al*. [15] indicated that the rim seal cavity, rather than the number of vanes and blades in the gas path, would determine the cell size, shape and speed of the flow structures. They showed that large unobstructed clearances would develop less (in number) but larger (in size) structures and vice versa. In a thorough study, Schädler *et al*. [9] concluded that the axial width of the vortical structure will be of the order of magnitude of the distance between stationary and rotating cavity discs.

Gao *et al*. [12] also pointed out that each experimental campaign may also be affected by protrusions in the cavity volume such as bolt heads [16], eccentricity in the experimental rig [17], vibrations and annulus flow conditioning components which could distort the recorded unsteadiness. Furthermore, the phenomenon was observed to be time-dependent with a high degree of randomness, which meant that each revolution would have different number and intensity of the flow structures, as noted by Cao *et al*. [6]. Beard *et al*. [16] provided clear evidence of this with their phase analysis methodology which captured how the phase lag for each pair of pressure measurements differed for each revolution within the same run.

The origin of the aforementioned rim seal pressure fluctuations continues to be investigated, predominantly through CFD studies. Three general trends stand out in the published literature pointing to the Taylor-Couette instability, Kelvin-Helmhotz instability or inertial waves as triggers. The study conducted by Gao *et al*. [12] revealed that the rim seal unsteady flow structures originate from the restoring inertial effects of the Coriolis forces, thus regarding them as inertial waves. In addition to the inertial waves, some studies have suggested the presence of aeroacoustic phenomena in the rim seal cavity. The full annulus LES unsteady computational study of Pogorelov *et al*. [18] showed the first numerical evidence of coexistence of acoustic and inertial modes in the cavity. Most of these investigations are numerical and at low rotational Mach numbers, therefore there is a need for more experimental research to verify and extend the findings of the computational studies. This is the objective of the current work.

EXPERIMENTAL SETUP

The results discussed in this paper were obtained at the upgraded Oxford Rotor Facility (ORF) described in detail by Bru Revert *et al*. [19]. The working section featured a chute rim seal arrangement with a reduced annulus casing line as shown in Figure 2. The purge flow was introduced into the stator-rotor cavity from the primary feed through the overlapping seal. Static pressure and total temperature measurements were taken in this region to check the flow conditions. Upstream rakes of total pressures and temperatures monitored the mainstream flow (when provided). Steady static pressure taps were installed in the stator wall of the rim seal cavity and the casing wall above the seal. A total of 11 ultra-miniature Kulite^{TM} XCQ-062 series unsteady pressure transducers were radially and circumferentially distributed in the cavity wall as shown in Figure 3. The pressure transducers of 50psiA and 100psiA (uncertainty of ±0.1% of the full scale) were mounted in the stator ring with no protrusions to avoid surface discontinuities.

Unsteady pressures and rotor disc speed were logged at 1MHz through the high speed channels of the NI PXI/SCXI data acquisition system. The output voltage of the Kulite^{TM} sensors was amplified by Fylde FE-579-TA amplifiers with an AC coupling circuit that allowed a maximum gain of 1000.

TEST MATRIX

Tests were conducted with three different mainstream flow configurations: no external flow (only purge flow), axial axisymmetric annulus flow and non-axisymmetric mainstream flow. The latter was achieved by introducing 36 reduced-span NGVs with an exit flow Mach number of 0.87 to generate a swirl component and pressure asymmetries in the annulus. No rotor blades were included. To allow comparison across experimental campaigns, the axial velocity was constant when mainstream flow was present. Full details of the experimental methodology are provided by Bru Revert *et al*. [19].

Unsteady pressure measurements inside the cavity were recorded in the radial and circumferential directions to explore the effect of non-dimensional (purge) mass flow, C_w (often replaced by the non-dimensional flow ratio $U_{\mathrm{m}}/(\Omega b)$), rotational Reynolds number, $\mathrm{Re}_{\emptyset}$, and mainstream flow configuration. The flow coefficient, $U_{\mathrm{ax}}/(\Omega b)$, is also included for reference. The bounds of the experimental test matrix are summarised in Table 1. These conditions were achieved in the experiments by varying rotor speed and purge flow rate for a fixed annulus mass flow. At nominal conditions, the non-dimensional absolute seal clearance of the chute rim seal was $s_{\mathrm{c}} = 0.0042$, measured perpendicular to the rotor platform.

DATA POST-PROCESSING

The Fast Fourier Transform (FFT) converted the time-dependent pressure signals into the frequency domain revealing the presence of distinct peaks from the unsteady flow structures rotating in the cavity. A window length of 4×10^4 was used to process the FFT, providing a frequency spacing of 25Hz. The amplitude of the spike is proportional to the intensity of the perturbance whilst the frequency relates to its angular speed and circumferential wavelength. The study by Beard *et al*. [16] showed that in absence of annulus flow the distinct frequency of the inertial waves was proportional to the rotor speed (and intensity of the disc pumping effect), with an approximately constant non-dimensional frequency $f/\Omega \sim 20$.

Previous studies have reported unsteady flow structures rotating around the annular seal cavity at a fraction of the rotor disc speed. These are regions of high and low pressure depicted as L lobes of ingress and egress separated an angle β in Figure 4. The flow structures from inertial waves rotate at an angular speed ω_{iw} in the same direction as the rotor disc, where ω indicates the rotating speed of the flow structures. The number of lobes and their travelling speed can be obtained from phase analysis. This consists of the cross-correlation of two time signals recorded from sensors spaced in the circumferential direction by a known angle α, providing the time lag Δt_{α}. The time (or phase) lag represents the time that a single flow structure took to rotate within the seal cavity by α degrees from one probe to the other. The angular velocity of the inertial wave is obtained from the circumferential spacing and the time as $\omega_{iw} = \alpha/\Delta t_{\alpha}$. The two sensors would log the same frequency $f = 2\pi/\Delta t_{\beta}$, where Δt_{β} is the time period between flow structures separated by an angle β as shown in Figure 4. The distance between the lobes can be obtained from $\omega_{iw} = \beta/\Delta t_{\beta}$, which then allows the number of lobes to be determined as $L = 2\pi/\beta$.

Cao *et al*. [6] pointed out that the high degree of randomness in the phenomenon leads to variations in the time lag and characteristics of the flow pattern from one revolution to the next. Common practice has assumed an average time lag value (Horwood *et al*. [13]), although Town *et al*. [15] highlighted the increased error when an average time lag is used (instead of the dominant time lag). Beard *et al.* [16]

introduced an alternative methodology that overcomes this inconvenience by plotting the time lag obtained at all rotor revolutions in a summary plot, as shown in Figure 5. The non-dimensional time lag in the x-axis, $\Delta t_\alpha \, \Omega/2\pi$, is provided by the cross-correlation of two signals spaced in the circumferential direction. The pairing of all the unsteady pressure sensors provides the 15 combinations visible in the y-axis. The area of the dots indicates the repeatability of the time lag across all revolutions.

The slope of the fitted trend lines identifies the angular speed of the flow structures, ω_{iw}. Parallel trend lines are plotted to capture the dots offset from the origin. The horizontal spacing is equal to the time period between flow structures, Δt_β, obtained from the peak frequency. The vertical spacing between the lines represents angle between flow structures, β, from which the number of lobes or nodal diameters is determined.

UNSTEADY CAVITY FLOW BEHAVIOUR

The flow in the stator-rotor cavity is analysed in the time and frequency domains before proceeding to the phase analysis.

Time domain

The specific capability of the data acquisition system did not allow the unsteady and steady pressures to be logged simultaneously. The cavity pressure coefficient from unsteady and steady pressure data acquired in different test runs are compared in Figure 6. Results in the three annulus flow configurations prove that the aerodynamics were repeatable, therefore any interpretation of the cavity flow field derived from the unsteady pressure measurements is consistent and directly applicable to the mean flow.

Please note unsteady pressure measurements were not available on the inclined wall of the stator ring.

Bru Revert *et al*. [19] previously reported that the change in geometry in the stator wall induced two vortical structures identified through different swirl velocities in the inner and outer regions of the cavity volume. This was observed as a change of slope in the radial distribution of the steady pressure coefficient at $r/b \sim 0.93$. Bru Revert *et al*. [20] also identified an increase in the amplitude of the FFT from the unsteady pressure signal at approximately this location, see Figure 6 d). The peak unsteadiness could be caused by the shear of the two coexisting vortices or flow separation of the radial inflow on the stator.

Frequency domain

The influence of purge supply, rotor disc speed and external pressure asymmetries is studied in this section based on the FFT of the signals obtained from the unsteady pressure sensors on the stator cavity wall. The results at the location of the circumferentially spaced sensors ($r/b = 0.96$) are summarised in Figure 7. Three characteristic frequencies can be observed depending on the operating conditions.

In absence of annulus flow, Figure 7 left, a clear isolated distinct peak appears in the frequency spectra. This corresponds to the frequency of the inertial waves, a rotationally-induced phenomenon strongly dependent on the rotational speed. The introduction of an external annulus flow increases the broadband unsteadiness and excites a band of frequencies at $f \sim$ 1000-1300Hz. Figure 7 displays this effect independently of the annulus flow swirl velocity and rotor disc speed. Indeed, it was still logged with a stationary rotor, and it was observed across different purge flow rates and seal clearances. The frequency remains constant throughout the different test cases examined but the amplitude of the unsteadiness is lowest for the rotationally-dominated situations (at higher rotational speed). An additional frequency at disc speed $f/\Omega \sim 1$ (67, 101, 131 and 150 Hz respectively) also stands out under the influence of any external annulus flow. The intensity of this peak can be stronger than that of the inertial waves at low rotor speeds. The source of this once-per-revolution phenomenon may lie in a slight rotor eccentricity as this frequency was not registered with a stationary rotor. A small shift in the inertial wave frequency peak was observed with a swirled annulus. However, it appeared to be more strongly dependent on rotor disc speed than annulus swirl, opposing the observations made by Cao *et al*. [6].

The spectrograms in Figure 8 present contour plots of unsteady pressure FFT for the highest rotor disc speed, $Re_{\emptyset} = 3\times10^6$. The frequency appears in the y-axis plotted against the rotor revolution number in the x-axis. The colour contour indicates the intensity of the pressure fluctuations through the amplitude of the FFT.

In absence of external flow, Figure 8 a), a clear band of high frequency content is identified at approximately $f \sim 3000$ Hz across all rotor revolutions. This excitation corresponds to the inertial waves and is consistent with the results of Beard *et al*. [16] which identified them at $f/\Omega \sim 20$. The introduction of an axial axisymmetric annulus flow, Figure 8 b), excites a highly energetic region at $f \sim 1100$ Hz. The band of frequencies related to the inertial waves is still visible at $f \sim 3000$ Hz, although it shows higher scatter and has been relegated to second most energetic phenomenon. The $f/\Omega \sim 1$ (150 Hz at

$Re_\phi = 3\times10^6$) excitation detected in the frequency spectra of Figure 7 is also observed in Figure 8. The overall unsteadiness and level of randomness increased with the introduction of NGVs in the main gas path, Figure 8 c). The same remarks from Figure 8 b) are applicable.

Phase analysis

The unsteady flow features in the rim seal cavity are further investigated through phase analysis of circumferentially distributed pressure signals. A Butterworth bandpass filter was used to discriminate the high amplitude low frequencies below $f/\Omega \sim 6$. Cross-correlation of all possible combination of circumferential unsteady pressure transducers (15 pairing possibilities) was calculated across all revolutions. Phase analysis plots were created following the methodology detailed by Beard *et al.* [16]. The time lag is non-dimensionalised by the time taken by the rotor to complete one revolution and shown in the x-axis. The y-axis includes the circumferential distance between the pressure transducers paired to cover different angles.

All results with no annulus flow indicated the presence of inertial waves with 27-29 lobes rotating at approximately 80% of rotor disc speed. An example phase analysis summary plot is shown in Figure 9 and is in agreement with similar test data presented by Beard *et al*. These values were replicated across the range of purge flows and rotor disc speeds studied. Very clear trend lines fit the data, consistent with Figure 5.

The introduction of flow in the gas path revealed the coexistence of three sets of rotating flow structures as identified in Figure 10. This is observed through the repeatability of the dominant time lag derived from cross-correlation of the different pairing combinations of time-dependent pressure transducers. Larger data scatter is visible comparing Figure 10 to Figure 9, consistent with the increase in broadband unsteadiness derived from the introduction of axial and swirled annulus flow already discussed in Figure 7 and Figure 8. Data in Figure 7-10 show three different ways of studying the same results: frequency spectra, spectrogram and phase analysis.

Focusing on Figure 10, inertial waves (red) with 27 lobes are indicated rotating at 76% of rotor disc speed. Solid trend lines (in green and blue) are also fitted to the two prominent phase bands. These provide values of angular velocity that indicate the existence of waves travelling faster than the rotor, at 1.6 and 2.1 times the disc speed. Physically, this can only occur if acoustic waves were present in the stator-rotor cavity. A forward or backward travelling acoustic wave rotating in the stator-rotor cavity would travel at $U_{\mathrm{aw}} \approx a \pm U_{\emptyset}$, where a is the speed of sound. Bru Revert *et al*. [19] demonstrated that the tangential flow velocity at the rim would be approximately half of rotor disc speed $U_{\emptyset}$=0.5(Ωb) under swirled annulus flow.

The dashed green and blue lines in Figure 10 show calculated acoustic wave speeds (assuming $a \sim 340$ m s^{-1}). Good agreement is found between the calculated and best fit forward (green) travelling acoustic wave. The repeated finer green lines are parallel to the bold green line indicate a nodal diameter of 9. These are at the same frequency as the inertial waves and only shown between -0.05 to 0.2. The repeated fine blue lines assume a backward travelling acoustic wave with 9 nodal diameters. The results suggest some possible activity in this mode but are not clear. There is no obvious connection of the backwards acoustic wave at speed -1.6 with the other features.

Similar backward travelling waves were detected for other cases with annulus flow and are discussed further below. Please note that lobes (inertial waves) and nodal diameter (acoustic waves) are used as equivalents to link the terminology of both fields.

Phase analysis plots for a constant purge mass flow rate and different rotor disc speeds are shown in Figure 11 for a stator-rotor cavity under swirled annulus flow. The results of the phase analysis are presented together with the frequency spectra to facilitate interpretation of the unsteady pressure data. The lowest disc speed case, Figure 11 a), reveals a backward travelling acoustic wave in isolation. The vertical spacing between the data band lines appears to be constant, $\beta \sim 80°$, across Figure 11 despite the wave speeds and frequencies (axial spacing) depending on disc speed. This suggests that a backward travelling acoustic wave of 4 or 5 nodal diameters is present in all cases. The frequency spectra in Figure 11 a) and b) confirm that there is no distinct FFT peak from inertial waves, and that the lower band of frequencies associated to external flow are most relevant. The blue dotted lines are drawn assuming U_{aw} = 340 m s^{-1} and a 5 ND wave. In all cases a reasonable fit to the data is shown, the largest mismatch is of 12%. The corresponding frequencies of these theoretical waves would be 1142 Hz, in agreement with the values in Figure 7, confirming that this feature is associated with the presence of annulus flow.

A further observation is that the frequency spectra show strengthening of the broadband unsteadiness as rotor speed reduces. This is consistent with the higher differential between purge and annulus flow swirl at lower speeds generating greater shear and unsteadiness.

The phase analysis plot at $Re_{\emptyset} = 2.1\times10^6$ is similar to that just described for $Re_{\emptyset} = 1.5\times10^6$, dominated by a backward travelling acoustic wave and no obvious inertial waves. There is, however, more scatter in the results than at the lowest disc speed. Considerably more data scatter is found in Figure 11 c), the highest disc speed, where the inertial waves distinct frequency peak is more intense than that of the acoustic phenomena. The backward travelling acoustic wave still prevails in the phase analysis plot, but there are signs of the inertial wave as well as a forward travelling acoustic wave. Figure 12 confirms this with the phase diagram obtained when the backward travelling acoustic wave frequency band is filtered out with a bandpass filter between 2400 and 4500 Hz. This indicates nodal diameters of 27 and 9 for the inertial and forward travelling acoustic wave, as was found for the axial axisymmetric annulus flow case in Figure 10. At higher disc speeds the phase analysis revealed forward travelling acoustic waves at the same or similar frequency as the inertial waves and an integer fraction of the inertial wave nodal diameter. A summary of the acoustic and inertial waves features is included in Table 2, highlighting those cases in which similar frequencies were found and acoustic resonance may occur. Examination of the phase diagrams at higher purge flow rates indicate that the acoustic wave speed is not affected by the purge flow rate but its intensity is. Stronger presence of the inertial wave was observed at higher flow ratios. The interaction between inertial and acoustic waves was found to be strongly dependent on the operating conditions: in absence of annulus flow, inertial waves dominate the frequency spectrum, with an axial mainstream flow the forward travelling acoustic wave prevails and the backward travelling acoustic wave is strongest under a swirled mainstream flow.

To the authors' knowledge these data provide the first experimental evidence of the coexistence of acoustic and inertial waves in the stator-rotor cavity.

The sealing performance map introduced by Bru Revert *et al*. [19] is included in Figure 13 to link the steady values of sealing effectiveness obtained in the same chute rim seal to the unsteady flow phenomena. The purpose of this is to identify any causal link between ingestion and the presence of waves. In Figure 13, black crosses correspond to experimental data under an axial axisymmetric annulus flow, whilst the colored data points were obtained from the non-axisymmetric gas path flow tests. Each color represents a different value of flow coefficient (or rotor disc speed) whilst each symbol relates to a value of purge flow. The sealing effectiveness for a chute seal calculated with the disc pumping correlation [21] is shown as a continuous black line in Figure 13. Therefore, each colored line indicates the sealing performance improvement with purge flow for a constant rotor disc speed, comparing to the purely rotationally-induced ingestion scenario in black.

Rotationally-induced ingestion was found to be most relevant at low flow coefficients, $U_{ax}/(\Omega b)$, achieved with high rotor disc speeds ($\mathrm{Re}_{\emptyset} = 3\times10^6$ in red). At these conditions, experimental values of sealing effectiveness approached those predicted by the analytical correlation for disc pumping derived by Chew [21]. Away from it, at high flow coefficients achieved with low rotor disc speeds ($\mathrm{Re}_{\emptyset} = 1.5\times10^6$ in blue), ingestion induced by the circumferential pressure asymmetries in the annulus dominated. In between these two lines, both rotational and circumferential pressure effects in the gas path are relevant in the regime of combined ingestion. The operating conditions of the phase analysis plots in Figure 10 and Figure 11 are included as a red cross and empty markers respectively in Figure 13. An increase of rotor disc speed (Figure 11 a) to c)) intensifies the disc pumping effect, inducing an improvement of sealing effectiveness at this purge flow rate. The reader is advised that sealing effectiveness data presented in Figure 13 corresponds to *r/b* = 0.99 although the same trends were observed at *r/b* = 0.96 where unsteady results have been examined in this paper. Cross-examination of Figure 11 and Figure 13 suggests that larger levels of ingestion are found when the shear between annulus and purge flows is most intense, inducing the fastest rotating acoustic waves, under pressure dominated ingestion ($Re_{\emptyset} = 1.5\times10^6$). Under rotationally-induced conditions, three different sets of rotating structures have been identified but no direct link between the presence of acoustic or inertial waves, speed or number of lobes and sealing performance have been identified. However, the increased shear and presence of acoustic waves may contribute to the rim seal not being fully sealed at high purge flow coefficients. More research is needed to further explore this effect.

CONCLUSIONS

The Oxford Rotor Facility was instrumented with circumferentially distributed unsteady pressure transducers mounted on the stator-rotor cavity static wall. This permitted the investigation of the unsteady phenomena developing in the rim seal region and cavity. Experiments were conducted over a wide range of operating conditions in which annulus flow configuration (without, with axial and with swirled mainstream), purge flow rate and disc speed were varied. With this approach, conditions of rotationally-induced, pressure-induced and combined ingestion were achieved.

The rotating flow structures in the rim seal were studied through the Fast Fourier Transform of the time-dependent pressure, the spectrogram of ensemble-averaged pressure signals across all rotor revolutions and phase analysis. The latter was obtained from cross-correlation of the pressure fluctuations of pairs of sensors, selected from 6 circumferential positions.

The frequency spectra showed the previously identified distinct peak corresponding to the inertial waves in absence of annulus flow. The introduction of main gas path flow excited an additional band of frequencies and increased the overall broadband unsteadiness. This was unrelated to the swirl of the annulus flow or presence of pressure asymmetries and was associated with 4 and 5 nodal diameter backward and 9 nodal diameter forward travelling waves by the phase analysis.

Under an axial annulus flow, despite the high purge flow supply, the rim seal was found to never achieve a sealing effectiveness of value 1. The operating point of Figure 10 is indicated as a cross that falls in this asymptotic region of sealing effectiveness below unity. A forward acoustic wave was detected at these conditions, although more research is needed to further explore whether this link is causal or casual. The potential for interaction with acoustic waves raises the question as to importance of Mach number in rim seal performance.

ACKNOWLEDGMENTS

The contributions of Peter Smout, Sebastiaan Bottenheim and Feng Gao are gratefully acknowledged as well as the technical support of the Osney Thermofluids Institute.

FUNDING

The authors would like to thank Rolls-Royce plc and Innovate UK for funding this research through the grant TSB 113076.

NOMENCLATURE

a	speed of sound, m s^{-1}
b	disc radius, m
C_p	cavity pressure coefficient, $= (p\text{-}p_{1112})/0.5\rho(\Omega b)^2$
C_w	non-dimensional purge flow rate, $= \dot{m}/\mu b$
f	frequency, Hz
g	rim seal gap size, m
L	number of lobes
$\dot{m}$	mass flow rate, kg s^{-1}
p	pressure, bar
$p_{\text{dyn, p}}$	peak dynamic pressure, $= 0.5\rho(\Omega b)^2$, bar
r	radius, m
$\mathrm{Re}_\emptyset$	rotational Reynolds number, $= \rho\Omega b^2/\mu$
s_c	seal clearance, $= g/b$
T	temperature, K
U	axial velocity, m s^{-1}
U_m	mean flow velocity through seal in r-z plane, $= \dot{m}/\rho 2\pi b s_c$, m s^{-1}

Greeks

α	angle between probes, deg

β	angle between flow structures, deg
ρ	fluid density, kg m^{-3}
ε	sealing effectiveness, $= \frac{CO_{2,stator} - CO_{2,annulus}}{(CO_{2,purge} - CO_{2,annulus})}$
Δt_α	time lag between probes, s
Δt_β	time lag between flow structures, s
ω	wave rotating speed, rad s^{-1}
Ω	rotor rotational speed, rad s^{-1}
μ	dynamic viscosity, Pa s

Subscripts

ax	axial component value
aw	acoustic wave
aw, f	forward travelling acoustic wave
bw, f	backward travelling acoustic wave
iw	inertial wave
∅	tangential component
0	total value

Abbreviations

AC	Alternating Current
CFD	Computational Fluid Dynamics

FFT	Fast Fourier Transform
LES	Large Eddy Simulation
ND	Nodal Diameter
NGV	Nozzle Guide Vane
ORF	Oxford Rotor Facility
3D	Three Dimensional

REFERENCES

[1] Bohn, D., Rudzinski, B., Sürken, N. and Gärtner, W., 2000, "Experimental and Numerical Investigation of the Influence of Rotor Blades on Hot Gas Ingestion Into the Upstream Cavity of an Axial Turbine Stage". *Proceeding of the ASME Turbo Expo 2000: Power for Land, Sea, and Air. Volume 3: Heat Transfer; Electric Power; Industrial and Cogeneration*. Paper No 2000-GT-0284. Munich, Germany, 2000, doi: 10.1115/2000-GT-0284

[2] Bohn, D., Rudzinski, B., Sürken, N. and Gärtner, W., 1999, "Influence of Rim Seal Geometry on Hot Gas Ingestion Into the Upstream Cavity of an Axial Turbine Stage". *Proceeding of the ASME Turbo Expo 1999: Power for Land, Sea, and Air. Volume 3: Heat Transfer; Electric Power; Industrial and Cogeneration*. Paper No 99-GT-248. Indianapolis, USA, 1999, doi: 10.1115/99-GT-248

[3] Hills, N.J., Chew, J.W. and Turner, A.B., 2002, "Computational and Mathematical Modeling of Turbine Rim Seal Ingestion". *J. Turbomach*, 124(2):306–315. doi: 10.1115/1.1456461

[4] Roy, RP, Xu, G, Feng, J, and Kang, S. "Pressure Field and Main-Stream Gas Ingestion in a Rotor-Stator Disk Cavity." *Proceedings of the ASME Turbo Expo 2001: Power for Land, Sea, and Air*. *Volume 3: Heat Transfer; Electric Power; Industrial and Cogeneration*. Paper No 2001-GT-0564, New Orleans, USA, 2001. doi: 10.1115/2001-GT-0564

[5] Smout, P. D., Chew, J. W. and Childs, P. R. N., 2002, "ICAS-GT: A European Collaborative Research Programme on Internal Cooling Air Systems for Gas Turbines". *Proceedings of the ASME Turbo Expo 2002: Power for Land, Sea, and Air, Volume 3: Parts A and B*. Paper No:2002-GT-30479, Amsterdam, The Netherlands, 2002.doi: 10.1115/GT2002-30479

[6] Cao, C., Chew, J.W., Millington, P.R., and Hogg, S.I., 2004, "Interaction of Rim Seal and Annulus Flows in an Axial Flow Turbine." ASME. *J. Eng. Gas Turbines Power*, October 2004; 126(4): 786-793, doi: 10.1115/1.1772408

[7] Roy, R. P., Feng, J., Narzary, D. and Paolillo, R. E., 2005, "Experiment on Gas Ingestion Through Axial-Flow Turbine Rim Seals". *J Eng Gas Turbines and Power*, 127(3):573–582. doi: 10.1115/1.1850499

[8] Julien, S, Lefrancois, J, Dumas, G, Boutet-Blais, G, Lapointe, S, Caron, J F and Marini, R. "Simulations of Flow Ingestion and Related Structures in a Turbine Disk Cavity". Proceedings of the ASME Turbo Expo 2010: Power for Land, Sea, and Air. Volume 4: Heat Transfer, Parts A and B. Paper No GT2010-22729. Glasgow, UK, 2010. doi: 10.1115/GT2010-22729

[9] Schädler, R, Kalfas, A I, Abhari, R S, Schmid, G and Voelker, S., 2017, "Modulation and Radial Migration of Turbine Hub Cavity Modes by the Rim Seal Purge Flow". ASME *J. Turbomach*., 139(1):011011. doi: 10.1115/ 1.4034416

[10] Chilla, M., Hodson, H., and Newman, D. (June 28, 2013). "Unsteady Interaction Between Annulus and Turbine Rim Seal Flows." ASME. *J. Turbomach*. September 2013; 135(5): 051024. doi: 10.1115/1.4023016

[11] Chew, J.W., Gao, F., and Palermo, D.M., 2018, "Flow mechanisms in axial turbine rim sealing." *Proc. Inst. Mech. Eng. Pt. C J. Mechan. Eng. Sci.*, doi: 10.1177/ 0954406218784612

[12] Gao, F., Chew, J. W., and Marxen, O., 2020. "Inertial waves in turbine rim seal flows". *Physical Review Fluids, 5*(2), p. 024802. doi: 10.1103/PhysRevFluids.5.024802

[13] Horwood, JTM, Hualca, FP, Wilson, M, Scobie, JA, Sangan, CM, & Lock, GD. "Unsteady Computation of Ingress Through Turbine Rim Seals." *Proceedings of the ASME Turbo Expo 2018: Turbomachinery Technical Conference and Exposition*. *Volume 5B: Heat Transfer*. Paper No GT2018-75321, Oslo, Norway, 2018. doi: 10.1115/GT2018-75321

[14] Horwood, J. T. M., Hualca, F. P., Wilson, M., Scobie, J. A., Sangan, C. M., Lock, G. D., Dahlqvist, J., and Fridh, J., 2020, "Flow Instabilities in Gas Turbine Chute Seals." ASME. *J. Eng. Gas Turbines Power*. February 2020; 142(2): 021019, doi: 10.1115/1.4045148

[15] Town, J, Averbach, M, & Camci, C. "Experimental and Numerical Investigation of Unsteady Structures Within the Rim Seal Cavity in the Presence of Purge Mass Flow." *Proceedings of the ASME Turbo Expo 2016: Turbomachinery Technical Conference and Exposition*. *Volume 2B: Turbomachinery*. Seoul, South Korea, 2016. doi: 10.1115/GT2016-56500

[16] Beard, P. F., Gao, F., Chana, K. S., and Chew, J., 2017. "Unsteady Flow Phenomena in Turbine Rim Seals." ASME. *J. Eng. Gas Turbines Power*. 2017 139(3): 032501, doi: 10.1115/1.4034452

[17] Savov, S. S., Atkins, N. R., and Uchida, S. (July 19, 2017). "A Comparison of Single and Double Lip Rim Seal Geometries." ASME. *J. Eng. Gas Turbines Power*. 2017, 139(11): 112601, doi: 10.1115/1.4037027

[18] Pogorelov, A, Meinke, M, & Schröder, W. "Large-Eddy Simulation of Turbine Rim Seal Flow." *Proceedings of the ASME Turbo Expo 2018: Turbomachinery Technical Conference and Exposition*. *Volume 2A: Turbomachinery*. Oslo, Norway. 2018. doi: 10.1115/GT2018-75022

[19] Bru Revert, A., Beard, P. F., Chew, J. W., Bottenheim, S. "Performance of a Turbine Rim Seal Subject to Rotationally-Driven and Pressure Driven Ingestion.", ASME. *J. Eng. Gas Turbines Power.* doi: 10.1115/1.4049858

[20] Bru Revert, A., Beard, P. F. and Chew, J. W. Flow and Ingestion in a Turbine Disc Cavity under Rotationally-Dominate Conditions. *Int. J. Turbomach. Propuls. Power 2021, 6, 29.* doi: 10.3390/ijtpp6030029

[21] Chew, J. W., 1991, "A Theoretical Study of Ingress for Shrouded Rotating Disc Systems With Radial Outflow," ASME. *J. Turbomach*., 113(1), pp. 91-97. doi: 10.1115/1.2927742

Figure Captions List

forward ($\omega_{aw,f}$) and backward ($\omega_{aw,b}$) travelling acoustic waves and dashed lines for acoustic waves calculated values

Fig. 11 Phase analysis and frequency spectrum for three operating conditions under swirled annulus flow: a) Re_{ϕ} = 1.5×10^6, b) Re_{ϕ} = 2.1×10^6 and c) Re_{ϕ} = 3×10^6

Fig. 12 Phase analysis with filtered frequencies under swirled annulus flow

Fig. 13 Sealing performance map with operating points from Figure 10 and 11 at *r/b* = 0.99

Table Caption List

Table 1:

	$U_m/(\Omega b)$	C_w	$U_{ax}/(\Omega b)$	Re_{ϕ}
No flow	0.01 – 0.11	820 – 4200	0	$1.5 - 3\times10^6$
Axial flow	0.01 – 0.65	850 – 40000	0.56 – 1.32	$1.5 - 3\times10^6$
Swirled flow	0.03 – 1.3	3500 – 30000	0.45 – 1.04	$1.5 - 3\times10^6$

Table 2:

$Re_{\varnothing}$	1.5×10^6	2.1×10^6	2.7×10^6	3×10^6
$\omega_{aw,f}/\Omega$	4.7	3.2	2.6	2.1
$\omega_{aw,b}/\Omega$	-3.9	-2.4	-2.1	-1.6
ω_{iw}/Ω	0.8	0.8	0.76	0.76
$L_{aw,f}$	9	9	9	9
$L_{aw,b}$	5	5	5	5
L_{iw}	27	27	27	27
$f_{aw,f}/\Omega$	42.3	28.8	**23.4**	**18.9**
$f_{aw,b}/\Omega$	19.5	12	10.5	8
f_{iw}/Ω	21.6	21.6	**20.5**	**20.5**

Figure 1:

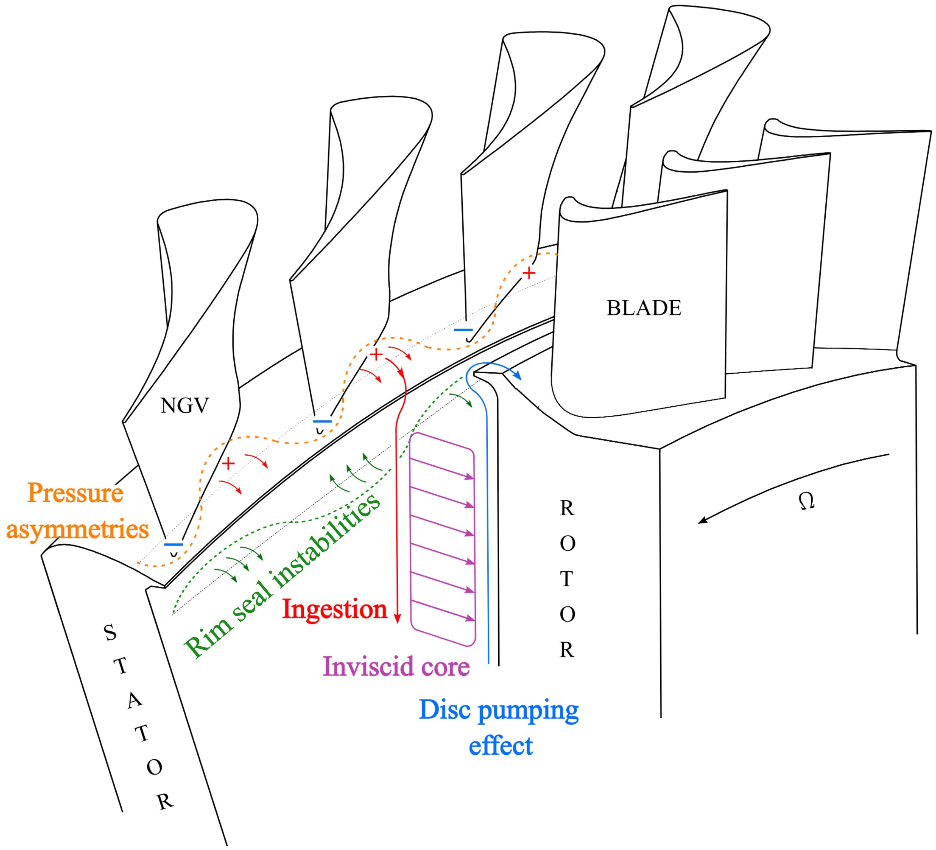
NGV
BLADE
Pressure asymmetries
Rim seal instabilities
Ingestion
Inviscid core
Disc pumping effect
STATOR
ROTOR
Ω

Figure 2:

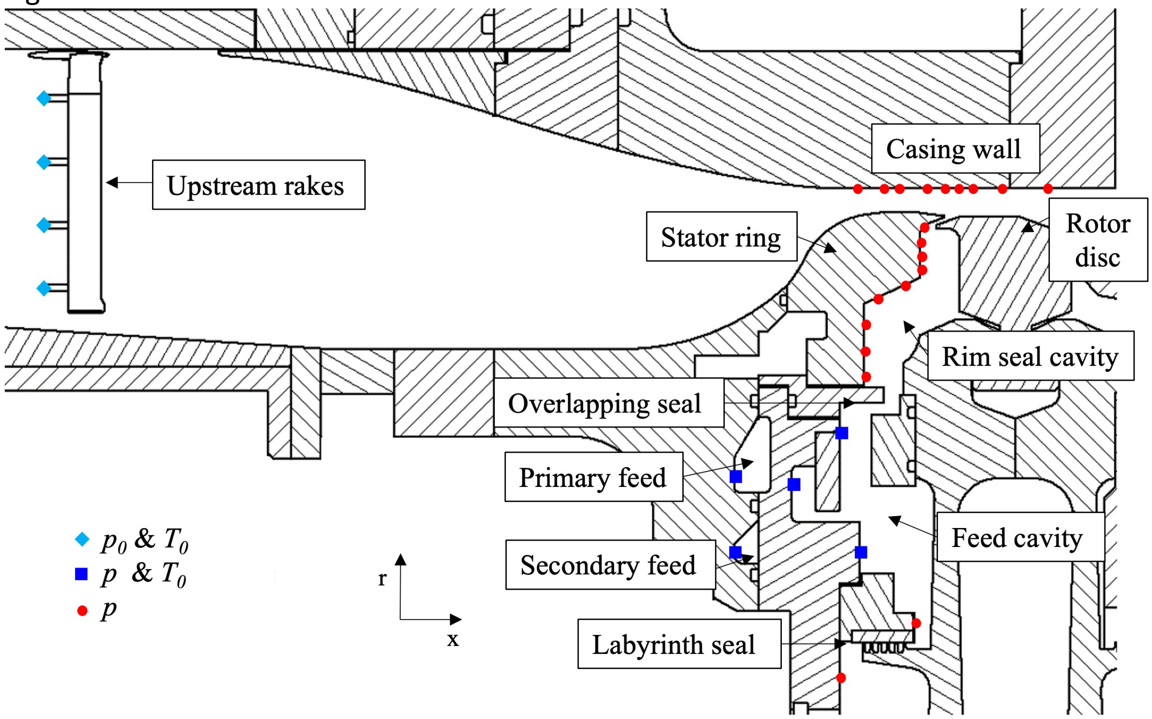
Upstream rakes
Casing wall
Stator ring
Rotor disc
Rim seal cavity
Overlapping seal
Primary feed
Feed cavity
Secondary feed
Labyrinth seal
p_0 & T_0
p & T_0
p
r
x

Figure 3:

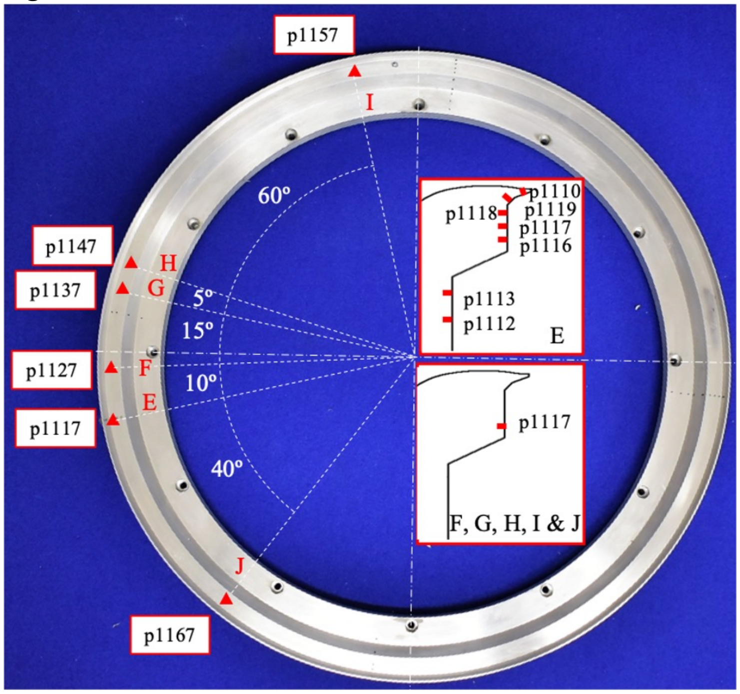
p1157
I
60°
p1110
p1118
p1119
p1117
p1116
p1147
H
p1137
G
5°
15°
p1113
p1112
E
p1127
F
10°
p1117
E
p1117
40°
F, G, H, I & J
J
p1167

Figure 4:

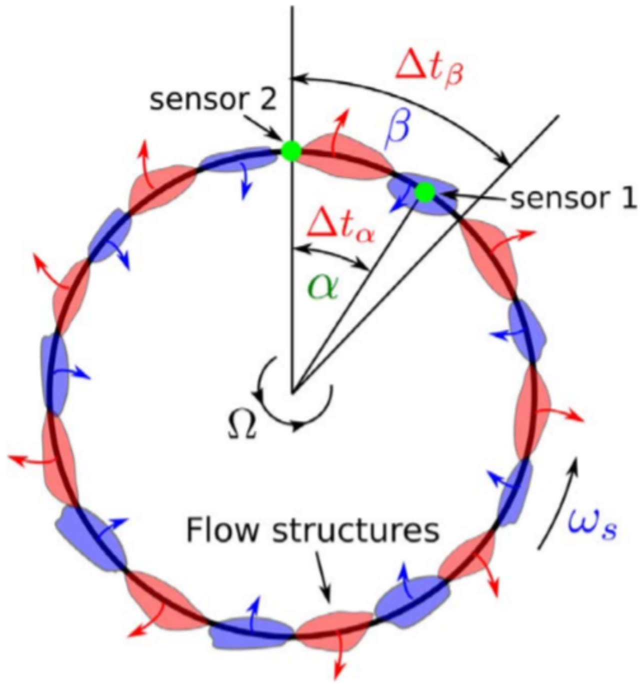

Δt_β
sensor 2
β
sensor 1
Δt_α
α
Ω
Flow structures
ω_s

Figure 5:

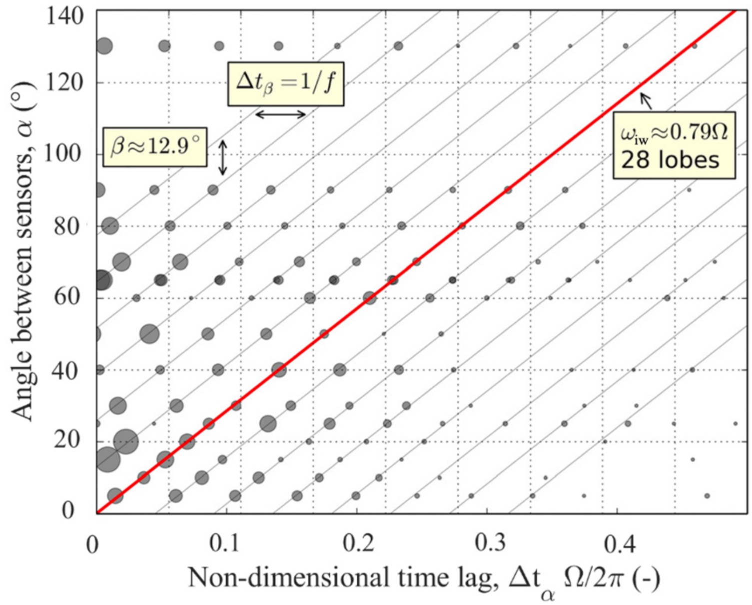

140
120
100
80
60
40
20
0
0
0.1
0.2
0.3
0.4
Angle between sensors, α (°)
Non-dimensional time lag, $\Delta t_\alpha\ \Omega/2\pi$ (-)
$\Delta t_\beta = 1/f$
$\beta \approx 12.9°$
$\omega_{iw} \approx 0.79\Omega$
28 lobes

Figure 6a:

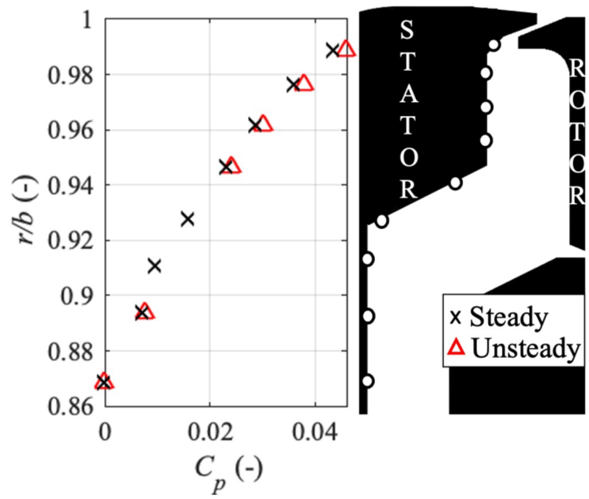

1
0.98
0.96
0.94
0.92
0.9
0.88
0.86
r/b (-)
0
0.02
0.04
C_p (-)
STATOR
ROTOR
Steady
Unsteady

Figure 6b:

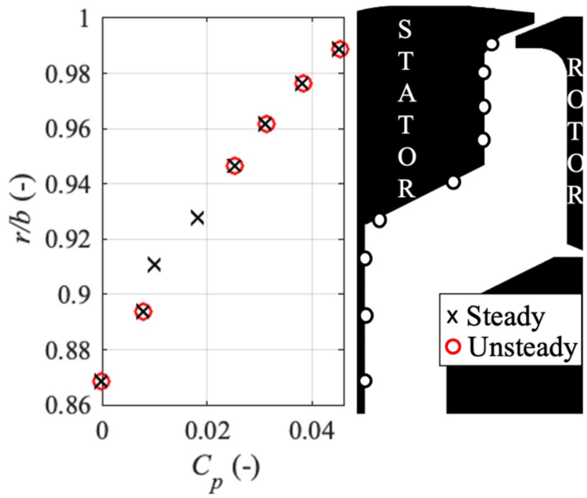
1
0.98
0.96
0.94
0.92
0.9
0.88
0.86
r/b (-)
0
0.02
0.04
Cp (-)
STATOR
ROTOR
Steady
Unsteady

Figure 6c:

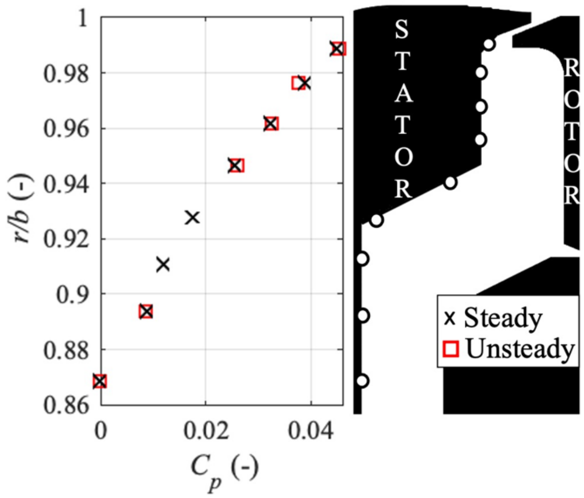
1
0.98
0.96
0.94
0.92
0.9
0.88
0.86
r/b (-)
0
0.02
0.04
C_p (-)
STATOR
ROTOR
Steady
Unsteady

Figure 6d:

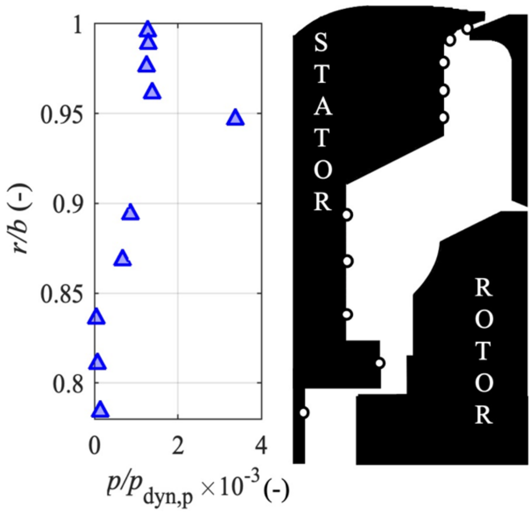

Figure 7:

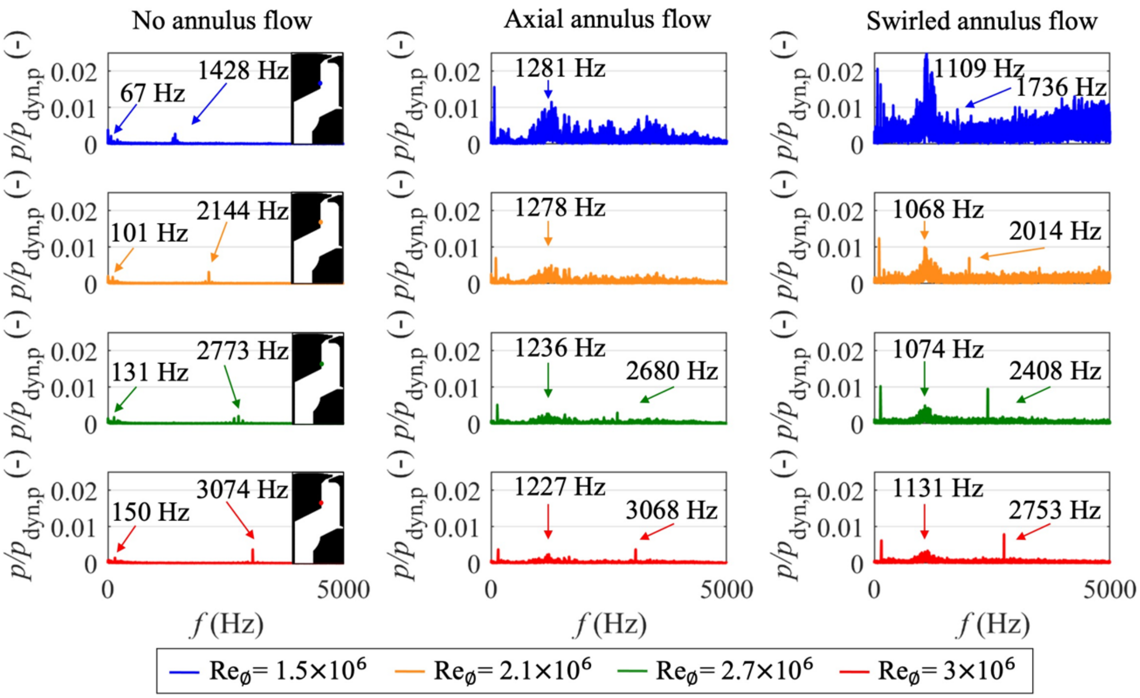
No annulus flow
Axial annulus flow
Swirled annulus flow
67 Hz
1428 Hz
101 Hz
2144 Hz
131 Hz
2773 Hz
150 Hz
3074 Hz
1281 Hz
1278 Hz
1236 Hz
2680 Hz
1227 Hz
3068 Hz
1109 Hz
1736 Hz
1068 Hz
2014 Hz
1074 Hz
2408 Hz
1131 Hz
2753 Hz
$p/p_{dyn,p}$ (-)
f (Hz)
$Re_\phi = 1.5\times10^6$
$Re_\phi = 2.1\times10^6$
$Re_\phi = 2.7\times10^6$
$Re_\phi = 3\times10^6$

Figure 8a:

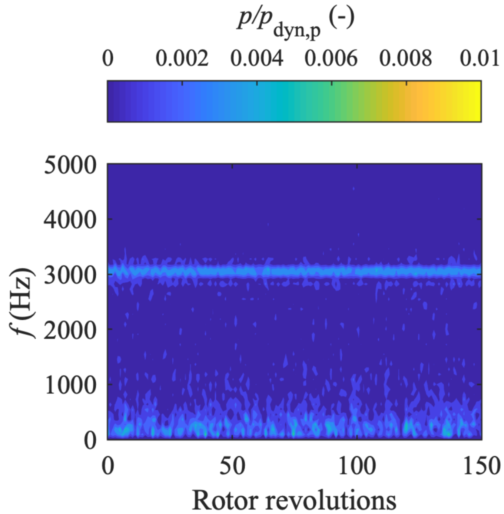
$p/p_{\mathrm{dyn,p}}$ (-)
0
0.002
0.004
0.006
0.008
0.01
5000
4000
3000
2000
1000
0
f (Hz)
0
50
100
150
Rotor revolutions

Figure 8b:

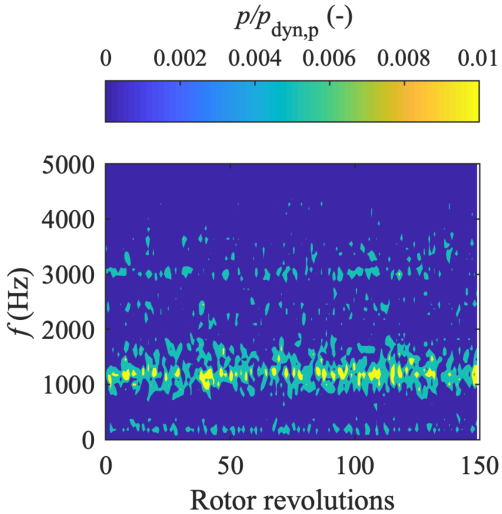
$p/p_{dyn,p}$ (-)
0
0.002
0.004
0.006
0.008
0.01
5000
4000
3000
2000
1000
0
f (Hz)
0
50
100
150
Rotor revolutions

Figure 8c:

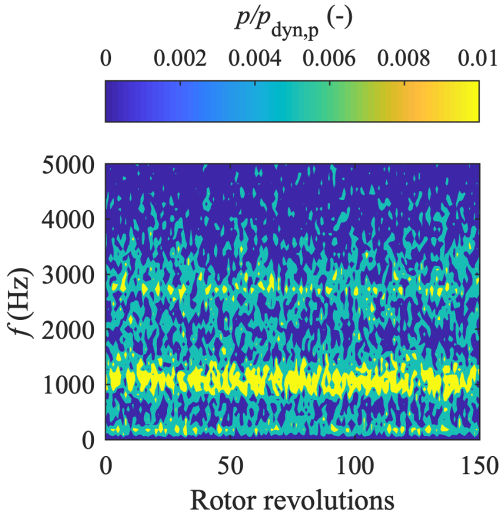
$p/p_{\mathrm{dyn,p}}$ (-)
0
0.002
0.004
0.006
0.008
0.01
5000
4000
3000
2000
1000
0
f (Hz)
0
50
100
150
Rotor revolutions

Figure 9:

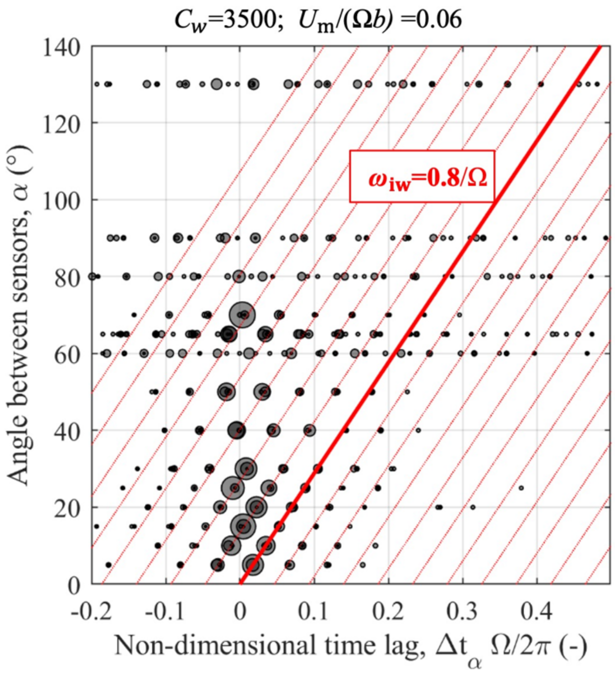

C_w=3500; $U_m/(\Omega b)$ =0.06
ω_{iw}=0.8/Ω
Angle between sensors, α (°)
Non-dimensional time lag, $\Delta t_\alpha\ \Omega/2\pi$ (-)
140
120
100
80
60
40
20
0
-0.2
-0.1
0
0.1
0.2
0.3
0.4

Figure 10:

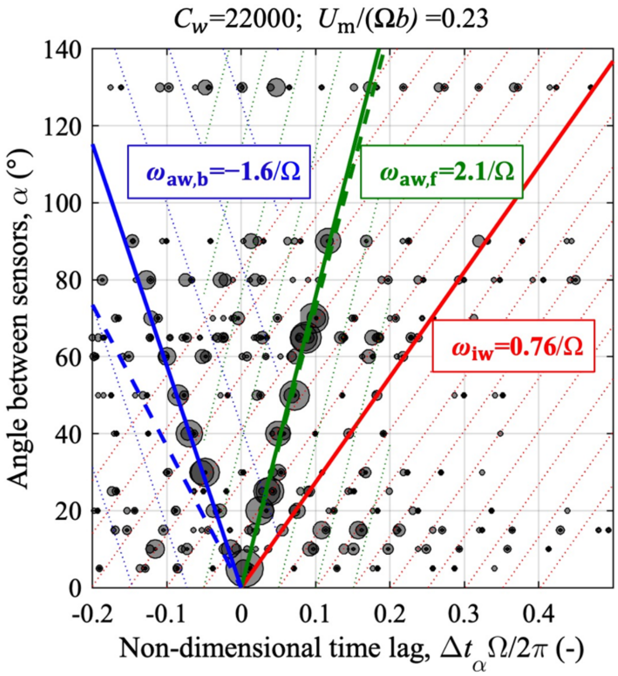

C_w=22000; $U_m/(\Omega b)$ =0.23
$\omega_{aw,b}$=−1.6/Ω
$\omega_{aw,f}$=2.1/Ω
ω_{iw}=0.76/Ω
Angle between sensors, α (°)
Non-dimensional time lag, $\Delta t_\alpha \Omega/2\pi$ (-)
0
20
40
60
80
100
120
140
-0.2
-0.1
0
0.1
0.2
0.3
0.4

Figure 11a:

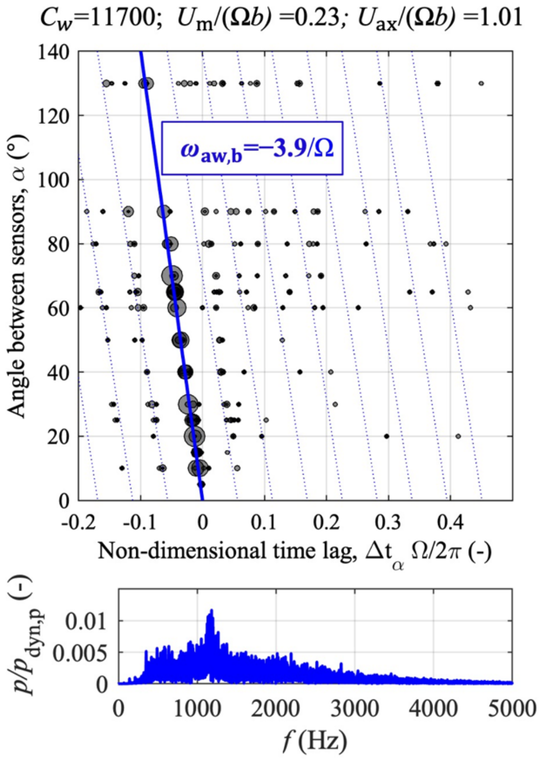
C_w=11700; $U_m/(\Omega b)$ =0.23; $U_{ax}/(\Omega b)$ =1.01
$\omega_{aw,b}$=−3.9/Ω
Angle between sensors, α (°)
Non-dimensional time lag, $\Delta t_\alpha\ \Omega/2\pi$ (-)
$p/p_{dyn,p}$ (-)
f (Hz)

Figure 11b:

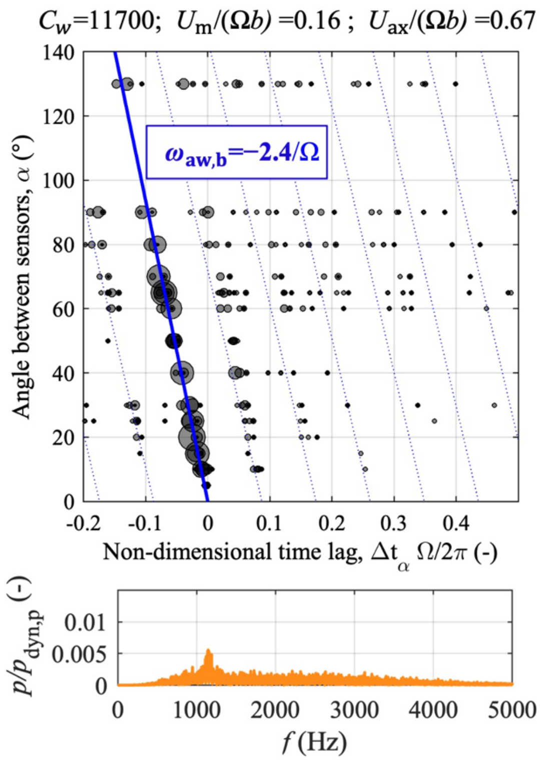
C_w=11700; $U_m/(\Omega b)$ =0.16 ; $U_{ax}/(\Omega b)$ =0.67
$\omega_{aw,b}$=−2.4/Ω
Angle between sensors, α (°)
Non-dimensional time lag, $\Delta t_\alpha\ \Omega/2\pi$ (-)
$p/p_{dyn,p}$ (-)
f (Hz)

Figure 11c:

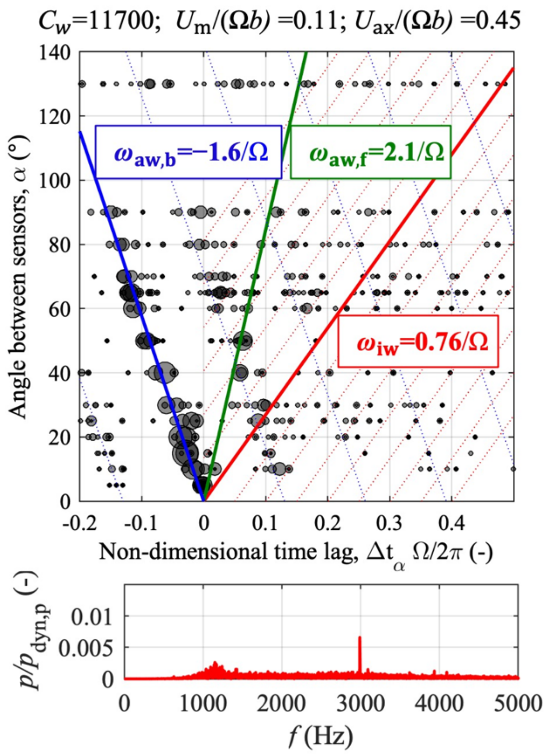
C_w=11700; $U_m/(\Omega b)$ =0.11; $U_{ax}/(\Omega b)$ =0.45
$\omega_{aw,b}=-1.6/\Omega$
$\omega_{aw,f}=2.1/\Omega$
$\omega_{iw}=0.76/\Omega$
Angle between sensors, α (°)
Non-dimensional time lag, $\Delta t_\alpha\ \Omega/2\pi$ (-)
$p/p_{dyn,p}$ (-)
f (Hz)

Figure 12:

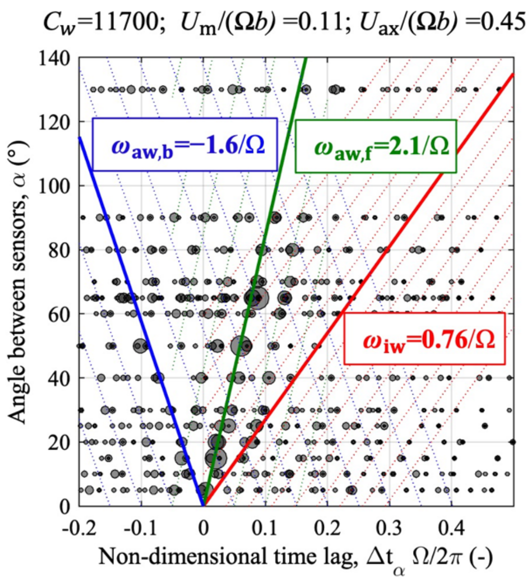
C_w=11700; $U_m/(\Omega b)$ =0.11; $U_{ax}/(\Omega b)$ =0.45
$\omega_{aw,b}$=−1.6/Ω
$\omega_{aw,f}$=2.1/Ω
ω_{iw}=0.76/Ω
Angle between sensors, α (°)
Non-dimensional time lag, Δt_α Ω/2π (-)
140
120
100
80
60
40
20
0
-0.2
-0.1
0
0.1
0.2
0.3
0.4

Figure 13:

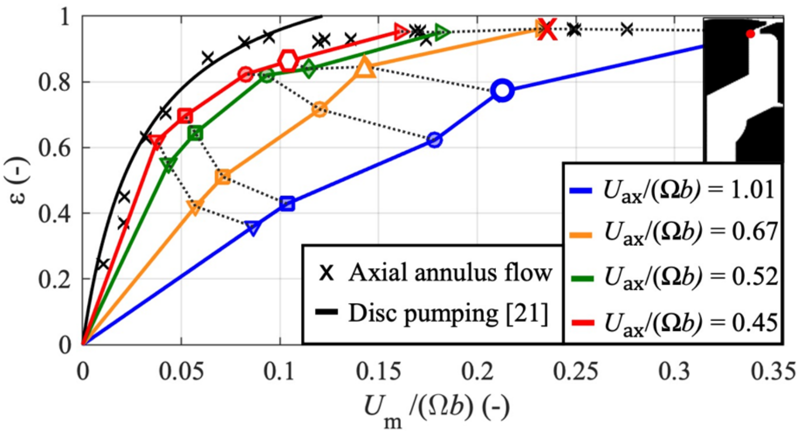

ε (-)
$U_m/(\Omega b)$ (-)
Axial annulus flow
Disc pumping [21]
$U_{ax}/(\Omega b) = 1.01$
$U_{ax}/(\Omega b) = 0.67$
$U_{ax}/(\Omega b) = 0.52$
$U_{ax}/(\Omega b) = 0.45$

